ACS APPLIED MATERIALS & INTERFACES

www.acsami.org

Research Article

A Spiral-Interlocking Microneedle Enabling Long-Term in Planta Glucose Monitoring

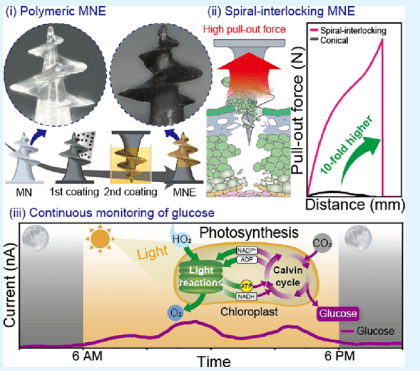
Chuljin Hwang,[#] Ju Hyeon Kim,[#] Hang Chan Jo, and Dae Yu Kim*

Cite This: *ACS Appl. Mater. Interfaces* 2026, 18, 53922−53934

Read Online

ACCESS | Metrics & More | Article Recommendations | Supporting Information

ABSTRACT: Continuous monitoring of plant metabolic dynamics remains challenging because existing sensing interfaces often fail to maintain stable mechanical coupling with deformable plant tissues during prolonged electrochemical measurements. Here, a spiral-interlocking microneedle electrode (SI-MNE) is presented for long-term in planta glucose monitoring through mechanically persistent tissue anchoring and minimally invasive biointerfacing. Unlike conventional conical or array-type microneedles that suffer from limited interfacial stability and motion-induced signal fluctuations, the SI-MNE employs a helical geometry that enables rotation-assisted insertion and 3D interlocking within plant tissue, thereby substantially enhancing mechanical retention. Cyclic-voltammetry-derived interfacial capacitance progressively increased during rotational insertion and reached a maximum under full-locking conditions, indicating enhanced electrochemical contact formation. Mechanical testing demonstrated approximately 10-fold higher pull-out resistance compared with conventional conical microneedles, while optical coherence tomography directly visualized stable insertion of the spiral architecture within plant tissue. To establish electrochemical glucose sensing functionality, a multilayer sensing interface consisting of a conductive carbon layer, PEDOT:PSS/Pt nanoparticle catalytic layer, and chitosan/glucose oxidase enzymatic layer was conformally integrated onto the spiral surface. The SI-MNE exhibited concentration-dependent amperometric glucose responses across 1−100 mM with a sensitivity of 350.3 nA/mM and high selectivity against representative plant sap interferents. The device further demonstrated stable operational reproducibility during continuous measurements and prolonged storage conditions. Using a three-electrode SI-MNE configuration, continuous glucose monitoring in living tomato plants successfully captured reproducible diurnal glucose fluctuations under natural light−dark cycles for 7 consecutive days without observable signal degradation or severe tissue damage. The proposed SI-MNE establishes a mechanically robust and electrochemically reliable biointerface for continuous metabolic monitoring in plants and provides a broadly applicable strategy for long-term in situ plant biosensing.



KEYWORDS: *spiral-interlocking, glucose sensor, plant microneedle, PEDOT:PSS, sugar template*

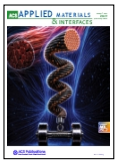
1. INTRODUCTION

Agriculture is central in global food security and supplying raw materials while driving economic development, particularly in developing regions.[1−3] In recognition of its global importance, the United Nations designated 2020 as the International Year of Plant Health, highlighting the need for sustainable strategies to support increasing food demands.[4,5] In this context, the Food and Agriculture Organization (FAO) has estimated that global agricultural productivity will need to increase by approximately 60% by 2050 to sustain a population approaching 10 billion, underscoring the importance of understanding and managing plant physiological processes.[6,7]

While metabolic monitoring is important for increasing agricultural efficiency, most existing monitoring strategies focus on environmental variables and/or macroscopic organism-level traits, providing indirect and limited insight into processes that govern plant growth and adaptation.[8,9] Because development is fundamentally regulated by cellular metabolism, direct interrogation of key metabolic intermediates offers more immediate and quantitative assays of physiological status.[10,11]

Among these metabolites, glucose is central. It not only serves as a primary carbon and energy source, but also functions in signaling to regulate photosynthetic activity, carbon allocation, and transcription.[12−17] Extensive prior studies have established that glucose signaling is tightly coupled with major phytohormone pathways, particularly ethylene, auxin, and cytokinin pathways, linking metabolic status with hormonal control of growth and development.[18−21] Consequently, temporal variations in tissue glucose concentration directly reflect metabolic

Received: May 24, 2026
Revised: August 28, 2026
Accepted: August 28, 2026
Published: September 23, 2026



Downloaded from pubs.acs.org/aamick/article-pdf/18/39/53922/6861346l/am-2026-10560b.pdf by INHA UNIV user on 19 October 2026

© 2026 American Chemical Society

https://doi.org/10.1021/acsami.6c10560
ACS Appl. Mater. Interfaces 2026, 18, 53922−53934

regulation and provide a sensitive indicator of growth status.[22−25]

Numerous techniques have been explored for glucose quantification, including mass spectrometry, Raman spectroscopy, chemiluminescence, fluorescence, and electrochemical methods.[26−29] Although they provide molecularly resolved readouts, they typically rely upon tissue disruption or active sap extraction, rendering them labor-intensive and perturbative to native plant physiology, while limiting long-term, real-time, and on-site measurements.[30−33] Moreover, intermittent sampling precludes monitoring transient and dynamic changes, resulting in fragmented representations of glucose dynamics.[9,34,35] Thus, there is a need for continuous glucose sensing. In this context, microneedle electrode (MNE)-based, wearable sensors are promising candidates for glucose detection, as they enable minimally invasive interfacing with internal sap streams, reduce tissue disruption, and support continuous in situ monitoring.[36−39] For example, Chen et al.[40] described hollow polymer microneedles with a platinum wire-based sensor interface for glucose monitoring, with a detection limit of 33 μM and sensitivity of 17 $nA{\cdot}\mu M^{-1}{\cdot}cm^{-2}$. Yun et al.[41] developed a clip-type, microneedle glucose sensor based on a non-enzymatic K−Co_3O_4 catalyst, with a 113 μM detection limit, that enabled direct glucose measurements in plant leaves under light−dark conditions.

However, conventional MNE-based sensors, particularly array-type designs, are limited by mechanical instability at the device−tissue interface because their multi-point insertion inherently disturbs tissue and creates motion-induced deformation, producing signal instability and measurement artifacts during in situ operation. In addition, conical MNE geometries provide limited mechanical engagement with plant tissue because their narrow curvature and reduced effective contact area hinder stable anchoring. As a result, maintaining stable attachment under ambient conditions remains challenging, ultimately limiting long-term, continuous plant glucose monitoring.

To address these issues, we developed a spiral-interlocking MNE (SI-MNE) with a mechanically engineered geometry for stable, in situ tissue glucose detection that supports continuous, in situ monitoring in plant tissues under natural light−dark cycles (Figure 1A). The SI-MNE was fabricated using a triethylene glycol dimethacrylate (TEGDMA)−diurethane dimethacrylate (DUDMA) monomer composite to achieve the interlocking geometry, followed by carbon spray coating to establish a conductive base layer. A multilayer electrochemical interface was subsequently constructed through sequential

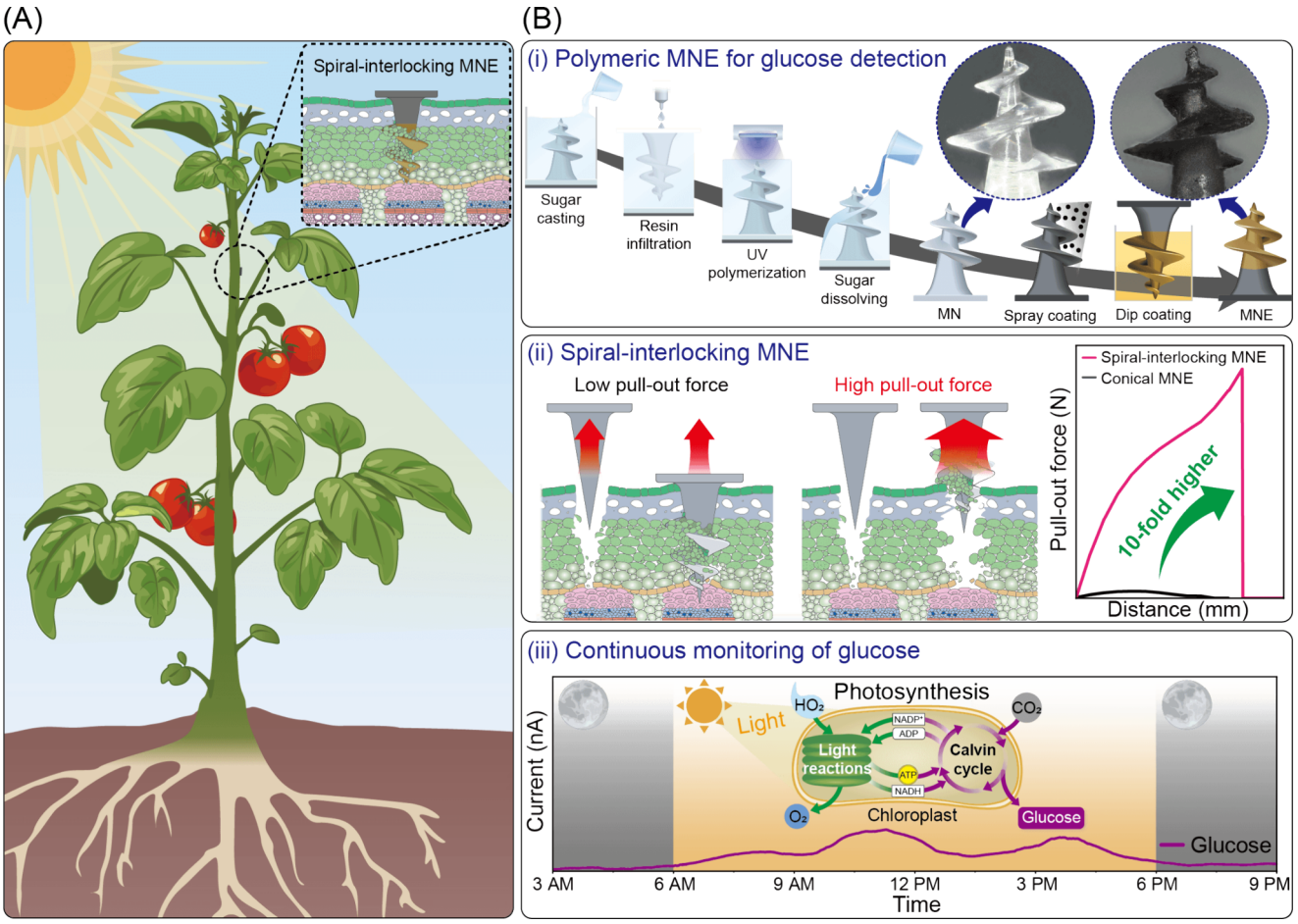


Figure 1. Overview of the SI-MNE for in situ glucose monitoring in plants. (A) Schematic illustration of the spiral-interlocking microneedle electrode (SI-MNE) inserted into plant tissue, enabling mechanically stable anchoring and reliable access to internal sap for continuous glucose sensing. (B) Fabrication and functional principles of the SI-MNE. (i) Stepwise fabrication of a polymeric MNE for glucose detection. (ii) Conceptual illustration of the spiral-interlocking geometry, highlighting increased axial pull-out resistance. (iii) Continuous in situ monitoring of glucose, showing temporal variations correlated with light−dark cycles and photosynthesis.

Downloaded from pubs.acs.org/aamick/article-pdf/18/39/53922/6861346l/am-2026-10560b.pdf by INHA UNIV user on 19 October 2026

https://doi.org/10.1021/acsami.6c10560
ACS Appl. Mater. Interfaces 2026, 18, 53922−53934

integration of a poly(3,4-ethylenedioxythiophene): polystyrene sulfonate/platinum (PEDOT:PSS/Pt) nanoparticle composite and a chitosan−glucose oxidase (GOx) layer, providing catalytic and enzymatic functionalities required for glucose sensing (Figure 1B(i)). Its spiral-interlocking geometry promotes mechanical interlocking with surrounding tissue, increasing resistance to axial extraction and enhancing interfacial mechanical retention (Figure 1B(ii)). Based on this mechanically stable configuration, the SI-MNE enables continuous in situ glucose monitoring, allowing real-time tracking of glucose dynamics in plant tissues under natural light−dark cycles. Stable glucose signal acquisition was maintained during prolonged operation for 7 days without observable signal degradation, demonstrating suitability for continuous plant glucose monitoring (Figure 1B(iii)). The SI-MNE developed in this study provides a new approach for continuous glucose monitoring in plants and offers a versatile foundation for developing next-generation in situ plant biosensors. Through comprehensive evaluation, this work establishes the feasibility of the developed minimally invasive sensing device for real-time glucose monitoring in plants.

2. MATERIALS AND METHODS

2.1. Materials and Reagents

DUDMA, TEGDMA, phenylbis (2, 4, 6-trimethylbenzoyl)phosphine oxide (photoinitiator), trichloro (1H,1H,2H,2H-perfluorooctyl)silane, chitosan, GOx (from *Aspergillus niger* type X-S), glutaraldehyde solution, fructose, lactate, sucrose, abscisic acid, salicylic acid, and isopropyl alcohol were purchased from Sigma-Aldrich (St. Louis, MO, USA). Conductive carbon spray (838AR total ground) was purchased from MG chemicals (Ontario, Canada), and Pt nanoparticles were purchased from US Research Nanomaterial, Inc. (Houston, TX, USA). PEDOT:PSS solution (Clevios PH 1000) was purchased from Heraeus (Hanau, Germany). Isomalt was purchased from Beneo-Palatinit (Germany). PDMS pre-polymer (Sylgard 184A) and curing agent (Sylgard 184 B) were purchased from Dow Corning Co., Ltd. (Shanghai, China). Deionized water (resistivity >18 MΩ cm at 25 °C) was utilized throughout the study.

2.2. Plant Materials and Growth Conditions

Tomato plants (*Solanum lycopersicum* var. cerasiforme) were cultivated in plastic pots (3.9 in × 3.9 in × 3.5 in) filled with a commercial potting soil mixture. Growth was conducted in a controlled plant growth device (Tiiun L023M2, LG Electronics Inc., Seoul, Korea) under long-day conditions (12 h light + 12 h dark). Daytime and nighttime temperatures were maintained at 25 °C and 22 °C, respectively.

2.3. SI-MNE Fabrication

A spiral MN master structure was fabricated using a two-photon polymerization 3D printer (Nanoscribe, Germany). A negative mold was then prepared by casting PDMS (pre-polymer and curing agent mixed at a 10:1 ratio) over the MN master, followed by thermal curing at 60 °C for 1 h. To reduce adhesion and facilitate mold release during subsequent replication, a PDMS-negative mold was treated with oxygen (O_2) plasma (30 W, 1 min; CUTE, Femtoscience, South Korea) and subsequently exposed to trichloro(1H,1H,2H,2H-perfluorooctyl)-silane vapor in a vacuum oven at 60 °C for 24 h, resulting in the formation of a superhydrophobic self-assembled monolayer (Figure S1A). Using this surface-modified PDMS mold, PDMS MNs were fabricated by casting a PDMS into the PDMS-negative mold followed by curing under controlled conditions (Figure S1B). The resulting PDMS MN structure served as a positive template for sacrificial mold preparation. Specifically, an aqueous isomalt solution was cast onto the PDMS MN under vacuum at 150 °C to form a rigid sugar mold, which was subsequently used as a sacrificial template for MN replication. After solidification, a precursor solution consisting of DUDMA and TEGDMA (2:8 ratio) with 1 wt % photoinitiator was introduced into the mold under a vacuum of 0.03 Torr to ensure complete infiltration. The structure was crosslinked via UV irradiation for 5 min (Model 18, Jetlight Company), and the final MN was obtained by dissolving the sugar template in water.

2.4. Surface Modification

A carbon spray coating was first applied to establish an electrically conductive current-collector layer on the SI-MN. On the resulting conductive surface, a PEDOT:PSS/Pt nanoparticle composite ink (250 mg/mL), homogenized by vortexing for 5 min, was deposited via an initial dip-coating process to form a conformal catalytic layer. Subsequently, a chitosan−GOx biocomposite was introduced through a second dip-coating step, yielding an enzymatic layer on the PEDOT:PSS/Pt-modified surface and completing the multilayer architecture. To immobilize GOx, the chitosan-coated SI-MN was immersed in a 2 wt % glutaraldehyde solution for 30 s, inducing covalent cross-linking within the chitosan matrix and stabilizing GOx on the MN surface.

2.5. Electrochemical Characterization during Rotational Insertion

CV measurements were conducted via electrochemical impedance spectroscopy (Interface 1010E, Gamry Instruments, USA) to quantify the electrochemical surface area (ECSA). A standard three-electrode configuration was adopted, using the MNE as the working electrode, a stainless-steel counter electrode, and an Ag/AgCl reference electrode. The potential window was set from 0 to 1.0 V with a scan rate of 100 $mV{\cdot}s^{-1}$. To characterize the influence of spiral rotation on interfacial charge accumulation, the rotation angle of the SI-MN was systematically changed from 360° to 2160° in 180° increments. The ECSA was subsequently estimated by integrating the non-faradaic double-layer region of the voltammograms, thereby capturing rotation-induced changes in the accessible surface area.

2.6. Pull-Out Force Measurement

The pull-out speed was controlled at 1 mm/s using a tensile-strain testing system (Mark-10 Corp., Hicksville, NY, USA). The tester applied a uniaxial extraction load during the pull-out process and continued the displacement until the MN detached completely from the petiole tissue.

2.7. Surface Characterization

Wettability was assessed using triplicate contact-angle measurements (Phoenix-MT, Surface Electro Optics, Co. Korea) from 4-μL water droplets. Images were processed using ImageJ software to ensure consistent contour extraction and angle determination. Morphology was characterized using scanning electron microscopy (S-4300SE, Hitachi) operated at 15-kV accelerating voltage. EDS was conducted on identical regions in samples to measure elemental compositions, providing spatial-distribution maps and elemental ratios for each layer. Chemical compositions and bonding states were measured using XPS (Nexsa-G2, Thermo Scientific) equipped with a monochromatic Al Kα source ($h\nu$ = 1486.6 eV), operating at 12 kV and 10 mA with a 400 μm spot size.

2.8. Optical Coherence Tomography

We employed a custom-built spectral-domain system to acquire cross-sectional tissue images, enabling direct visualization of interface geometry (Figure S2). The system was equipped with a broadband superluminescent diode (SLD; MT840-HP, Superlum, Carrigtohill, Ireland) operating at a central wavelength of 840 nm with a spectral bandwidth

Downloaded from pubs.acs.org/aamick/article-pdf/18/39/53922/6861346l/am-2026-10560b.pdf by INHA UNIV user on 19 October 2026

https://doi.org/10.1021/acsami.6c10560
ACS Appl. Mater. Interfaces 2026, 18, 53922−53934

of 100 nm, corresponding to a theoretical axial resolution of 3.1 μm in air. Lateral resolution was estimated to be 12.5 μm, from the beam diameter (2.5 mm) and focal length (50 mm) of the imaging probe. The SLD emitted a broadband optical power of 1.56 mW, of which 1.4 mW was delivered to the sample arm through a 90:10 fiber coupler. Interference signals were generated during the superposition of mirror-reflected light from the reference arm and backscattered light originating from scattering structures within tissues. Interferometric signals were recombined at the fiber coupler and directed to a custom-built spectrometer incorporating a line-scan camera (spL4096-140km, Basler, Ahrensburg, Germany). The resulting interference fringe patterns were transferred using a CameraLink frame grabber (PCIe-1433, National Instruments, Austin, TX, USA) and processed to reconstruct cross-sections of the MN−tissue interface.

2.9. In Vitro Glucose Measurements

Measurements were conducted using a conventional three-electrode configuration controlled by an electrochemical workstation, with potential resolution of 10 μV and current sensitivity of 10 pA. An Ag/AgCl electrode served as the reference electrode, with a carbon-coated polyethylene terephthalate sheet as the counter electrode. Chronoamperometric measurements were conducted in PBS at an applied potential of 0.5 V, with continuous stirring at 100 rpm.

2.10. In Plant Glucose Measurements

An SI-MNE glucose sensor was inserted into a tomato petiole under controlled environmental conditions. The amperometric current was continuously recorded for 12 h during the light phase and for an additional 12 h during the dark phase. The photoperiodic cycle was regulated via illumination with a light-emitting diode within a sealed dark chamber, enabling precise control of the light and dark phases during the monitoring period.

3. RESULTS AND DISCUSSION

3.1. SI-MNE Design and Fabrication

For high-fidelity fabrication of the proposed geometry, a sacrificial sugar-based templating strategy was employed. It enabled accurate replication of the three-dimensional helical features, followed by dissolution of the sugar template after curing to release the MNE. Figure 2A provides an overview of the design and fabrication process, and Figure S3 provides detailed geometric parameters. The electrode had an overall height of 830 μm and a base width of 550 μm (Figure S3A). The detailed side view (Figure S3B) shows five helical segments with radial

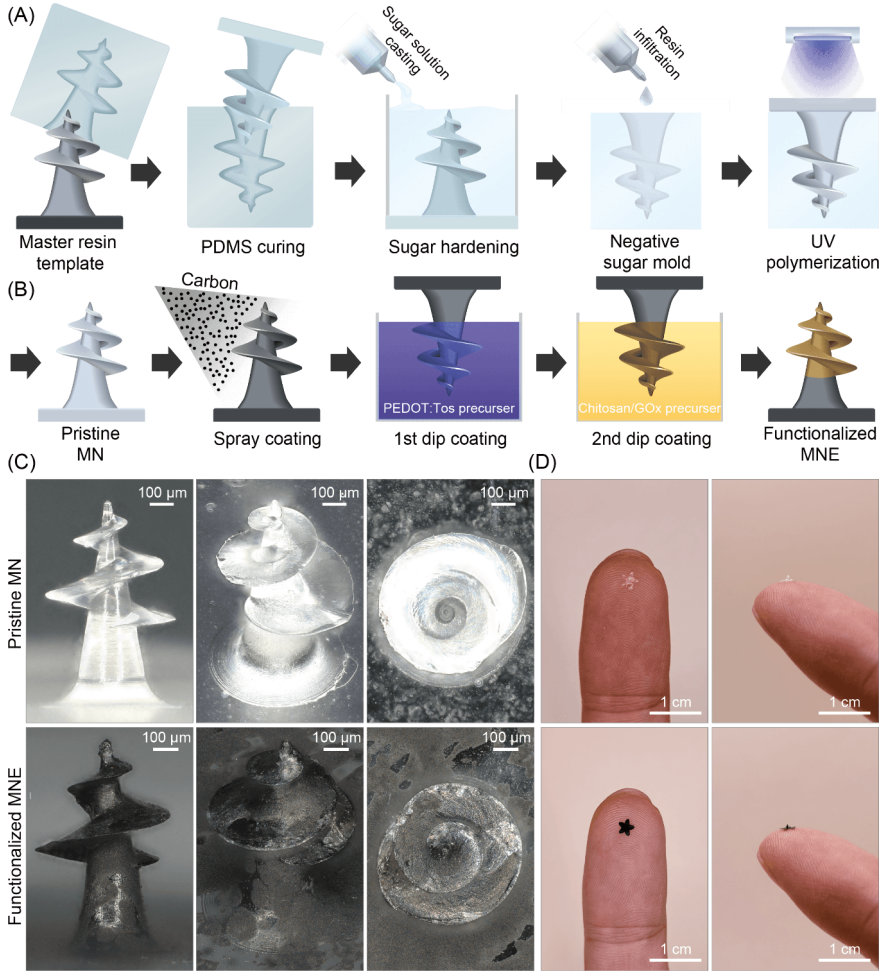


Figure 2. Fabrication and multilayer functionalization of the SI-MNE. (A) Fabrication schematic. (B) Stepwise surface functionalization of the pristine MNE, including carbon spray coating as a conductive base layer, followed by dip coating with a PEDOT:PSS/Pt precursor and chitosan/GOx precursor to establish an enzymatically active electrode interface. (C) Representative micrographs of pristine and functionalized MNE (side, oblique, and top views), with a surface morphology after multilayer surface modification. (D) SI-MNE integrated onto a star-shaped polyethylene terephthalate (PET) substrate.

Downloaded from pubs.acs.org/aamick/article-pdf/18/39/53922/6861346l/am-2026-10560b.pdf by INHA UNIV user on 19 October 2026

https://doi.org/10.1021/acsami.6c10560
ACS Appl. Mater. Interfaces 2026, 18, 53922−53934

extensions of 230, 185, 140, 88, and 32 μm and corresponding axial dimensions of 116.7, 94.3, 69.8, 43.2, and 16.3 μm, respectively. The top view (Figure S3C) shows a total spiral rotation of 810°.

Figure 2B illustrates the surface-modification steps applied to the SI-MNE. Initially, the pristine MNE surface was coated with conductive carbon to establish an electrically active base. Next, a PEDOT:PSS/Pt layer was deposited using dip coating to form a continuous conducting polymer interface. Finally, a chitosan matrix with incorporated GOx was applied to provide enzymatic functionality. This strategy provides a multilayered sensing interface.

The morphological characteristics associated with surface modifications are shown in Figure 2C. Optical micrographs were acquired from the side, oblique, and top views, then compared with those of pristine and functionalized SI-MNE. The pristine MNE was transparent with a clearly defined helical profile. After surface functionalization, the surface was darkened, indicating coverage, whereas the spiral morphology remained intact. Figure 2D shows an image of an individual SI-MNE integrated onto a star-shaped polyethylene terephthalate substrate for scale.

3.2. Rotational SI-MNE Insertion

Insertion was divided into three regimes according to degree of interaction between the electrode and surrounding tissue (Figure 3A). During the lock-initiation stage (i) (0−360°), the leading spiral gradually penetrated the outer epidermal layer while establishing initial mechanical engagement with cortical tissue. Continued rotation advanced the SI-MNE into a fully locked stage (ii) (360−1440°), in which the spiral conformed tightly to the surrounding parenchyma, capable of sustaining axial and torsional stresses. Further rotation produced over-rotation (iii) (>1440°), displacing tissue and reducing stable contacts.

To assess insertion quality, cyclic voltammetry (CV) was performed. CV profiles were used to extract interfacial capacitance, presented as a function of the rotation angle in Figure 3B, with representative CV curves shown in Figure S4. Capacitance increased progressively during lock

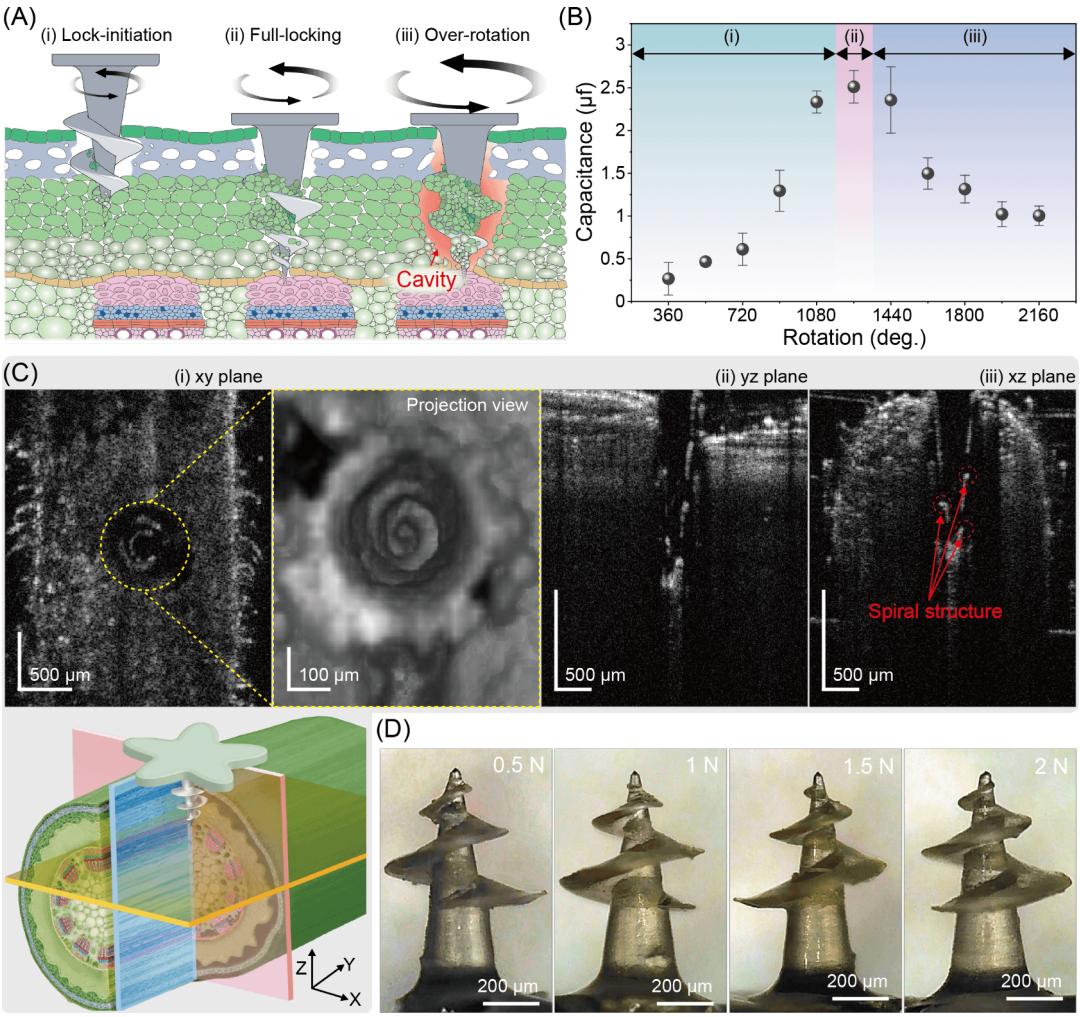


Figure 3. Controlled insertion and interlocking behavior of the SI-MNE in plant tissue. (A) Schematic illustration of the rotational insertion process. (i) Lock-initiation: the spiral leading edge penetrates the outer epidermal tissue, establishing the initial mechanical engagement. (ii) Full-locking: continued rotation enabled conformal anchoring of the SI-MNE within the cortical parenchyma. (iii) Over-rotation: excessive rotation induced localized tissue disruption and cavity formation around the insertion site. (B) Cyclic voltammetry-based insertion analysis, showing progressive increases in capacitive current as the rotation advanced from 360° to 2160°. (C) OCT images of SI-MNE insertion in plant tissue across (i) *xy*, (ii) *yz*, and (iii) *xz* planes. (D) Optical images of SI-MNE under increasing insertion forces (0.5−2 N), showing no structural deformation.

https://doi.org/10.1021/acsami.6c10560
ACS Appl. Mater. Interfaces 2026, 18, 53922−53934

Downloaded from pubs.acs.org/aamick/article-pdf/18/39/53922/6861346l/am-2026-10560b.pdf by INHA UNIV user on 19 October 2026

initiation (i), indicating an increase in the effective electrode–tissue interface. Because the radial dimensions of the spiral increase from the tip toward the base, the increase in capacitance became more pronounced as the larger spiral segments engaged the surrounding tissue. Capacitance peaked under the full-locking condition (ii), indicating that the largest effective interface had formed. As expected, further rotation led to decreased capacitance, consistent with cavity formation in the surrounding tissue.

Reliable assessment of SI-MNE insertion is challenging when performing surface optical observations alone, owing to the complex three-dimensional spiral-interlocking geometry. This produces depth-dependent features and overlapping interfaces within tissues, obscuring true insertion depth and spatial orientation when viewed externally. To address these limitations, optical coherence tomography (OCT) was employed, revealing distinct scattering patterns produced by the helical architecture. As the MNE is optically transparent, OCT contrast primarily was generated by tissue−tissue and tissue−MNE interfaces. These signals were interpreted based on light-penetration images along the spiral, illustrated in Figure S5. To validate these findings, OCT datasets were reconstructed into *xy*, *yz*, and *xz* orthogonal planes, providing multi-angle views of the MNE−tissue interface. Figure 3C presents representative cross-sectional and projection views, including *xy*-plane images (Figure 3C(i−ii)) that clearly show the helical profile. Finally, depth-resolved *xy*-plane slices at different z-axis positions (Figure S6) exhibited systematic scattering variations consistent with the spiral insertion path. These volumetric observations confirmed that SI-MNE insertion into plant tissues was precisely and spatially controlled.

To assess the mechanical response of the SI-MNE under insertion loads, axial compression was measured (Figure S7). A controlled normal load was applied along the SI-MNE axis while deformation was monitored by imaging. The compression test was conducted under axial loading without rotational insertion to evaluate the structural robustness of the SI-MNE. The spiral retained its overall geometry under 0.5−2 N of compression (Figure 3D). Only minor elastic deformation occurred at the outer spiral segments across this range, with no evidence of fracture, collapse, or permanent deformation. In summary, cyclic voltammetry, OCT imaging, and mechanical characterization consistently showed that the SI-MNE maintains its geometry upon insertion into plant tissue.

3.3. Spiral Geometry Enhances Tissue Interlocking and Pull-Out Resistance of SI-MNE

Figure 4A compares the insertion and pull-out behavior of a conventional conical MNE and the SI-MNE. Owing to its geometry, a conventional MNE provides limited engagement with surrounding tissue during axial loading, resulting in a lower force required for extraction. In contrast, the SI-MNE promotes interlocking, increasing resistance to extraction. This difference is reflected in the pull-out forces shown in Figure 4B and Figure S8, corresponding to an approximately 10-fold increase. Although these results demonstrate enhanced axial retention, practically one must allow for mechanical deformation produced by growth or external perturbations. Accordingly, we performed pull-out tests under controlled bending (Figure 4C). The bending radii varied from −10 and −2 mm (negative bending) to 2 and 10 mm (positive bending). The SI-MNE exhibited similar pull-out forces across all radii (0.185−0.212 N), with no noticeable reduction relative to the unbent state, indicating stability.

To complement the pull-out measurements, we compared axial retention under loads of 20 g (Figure 4D and Movie S1). The conical MNE was readily extracted from the tomato petiole, whereas the SI-MNE sustained the applied load. Further examination of the SI-MNE after removal showed that straight axial pull-out without rotational release resulted in tissue adhering to the spiral surface, whereas rotational pull-out preserved a clean spiral morphology (Figure S9). These observations collectively confirm robust mechanical engagement between the spiral-interlocking geometry and surrounding tissue during non-rotational extraction.

3.4. Stepwise Surface Characterization of SI-MNE

Reliable glucose detection relies on controlled surface modification, which directly governs electron-transfer efficiency and enzyme immobilization at the MNE surface. Surface engineering critically influences electrochemical performance by elemental composition and chemical bonding states. Accordingly, our sequential surface-modification steps were characterized using water-contact angle (WCA) measurements, energy-dispersive X-ray spectroscopy (EDS), and X-ray photoelectron spectroscopy (XPS) to track the evolution of surface wettability, elemental distribution, and chemical bonding at each coating stage. Morphological differences were visualized via optical microscopy (Figure 5A), revealing gradual changes in surface texture and coloration. Variations in surface wettability were evaluated through WCA measurements, corresponding results are shown in Figure 5B and summarized in Table S1. Each value represents the mean ± standard deviation obtained from at least three measurements. The UV-cured TEGDMA−DUDMA (pristine) film exhibited a WCA of 89.44 ± 0.89°, reflecting a moderately hydrophilic surface.[42]

Subsequent surface coatings led to a progressive increase in hydrophilicity: 72.41 ± 0.40° for carbon-coated, 57.28 ± 1.18° for the PEDOT:PSS/Pt-composite, and 49.38 ± 2.22° for the chitosan/GOx surface.[43,44] This consistent decrease reflects the progressive formation of increasingly hydrophilic surfaces accompanying each coating step, including the chitosan/GOx enzyme immobilization.[45]

To further analyze our surface modifications, we measured elemental distribution using EDS (Figure 5C). The carbon-coated surface (i) exhibited a uniform distribution of C and O. Following the PEDOT:PSS/Pt coating (ii), distinct Pt and S signals were observed, confirming that Pt was incorporated within the matrix. Following chitosan/GOx functionalization (iii), we detected increased N and O signals, accompanied by decreased Pt and S signals, consistent with covering of the PEDOT:PSS/Pt surface.

Similar results were observed using XPS (Figure 5D). For binding-energy calibration, the C−C peak of the carbon-coated surface at 283.7 eV was used as an internal reference. The C−C components of the PEDOT:PSS/Pt- and chitosan/GOx-modified surfaces were subsequently aligned to the same reference energy, as shown in the high-resolution C 1s spectra in Figure S10. After calibration, the survey spectra indicated characteristic peaks at binding energies of 283.7 eV (C 1s), 531.1 eV (O 1s), 399.1 eV (N 1s), 167.1 eV (S 2p), and 74.1 eV (Pt 4f), confirming the stepwise deposition of the PEDOT:PSS/Pt and chitosan/GOx layers. High-resolution XPS spectra of the coated PEDOT:PSS/Pt composite layer

Downloaded from pubs.acs.org/aamick/article-pdf/18/39/53922/6861346l/am-2026-10560b.pdf by INHA UNIV user on 19 October 2026

https://doi.org/10.1021/acsami.6c10560
ACS Appl. Mater. Interfaces 2026, 18, 53922−53934

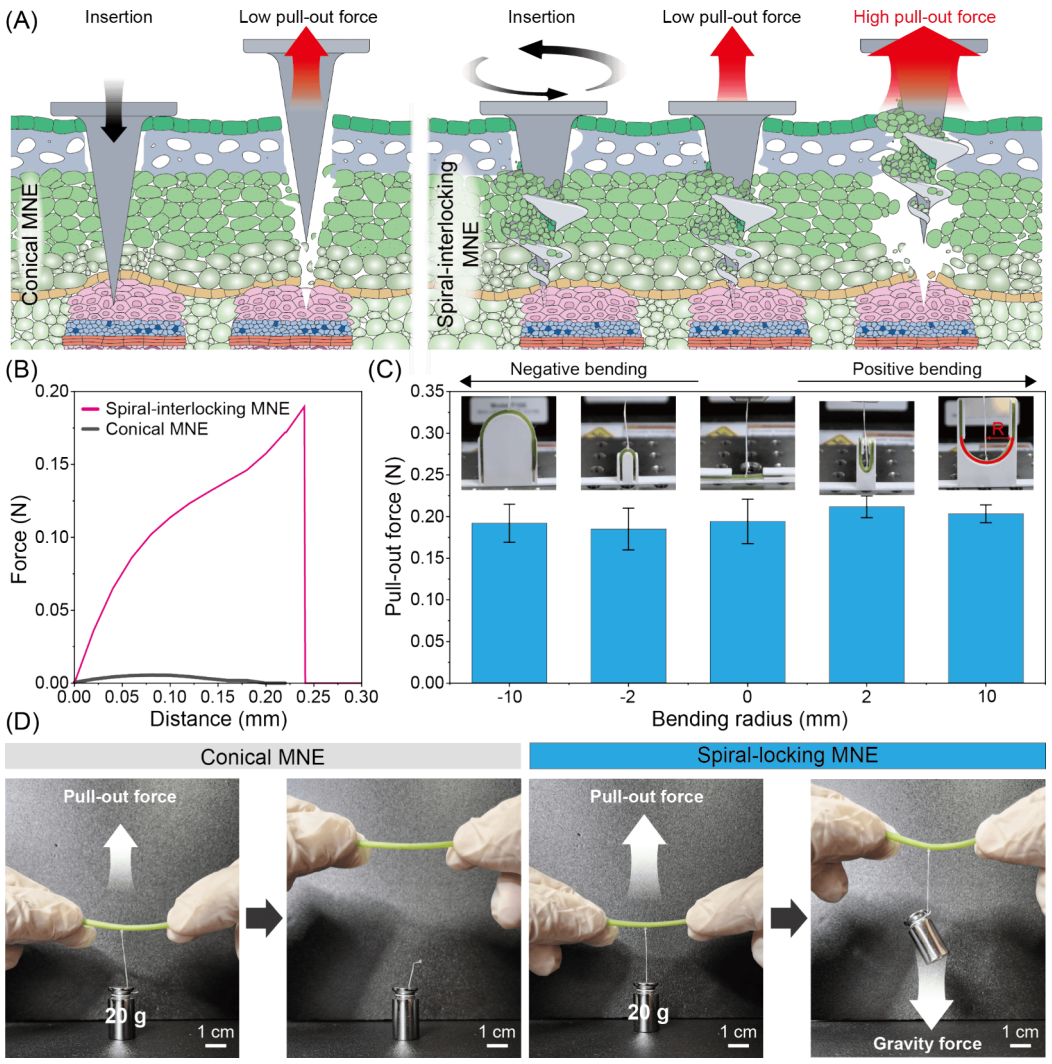


Figure 4. Mechanical robustness and anchoring behavior of the SI-MNE. (A) Schematic comparison of insertion and pull-out between a conical (left) and spiral (right) MNE. (B) Comparison of forces required to extract conical and spiral MNE from plant stems. (C) Pull-out force measured under varying bending radii, demonstrating stable mechanical performance under both negative and positive bending conditions. Error bars represent standard deviations. (D) Representative photographs of axial pull-out response of conventional conical and spiral MNE under identical loads of 20 g.

revealed information on the chemical states of sulfur and platinum. The S 2p spectrum (Figure 5E) exhibited a characteristic spin–orbit–spin doublet and was fitted using a Gauss–Lorentz function to resolve individual sulfur species.[46] Peak deconvolution resolved components at 163.4/164.7 eV and 167.7/169.0 eV, corresponding to the thiophene S moiety in PEDOT and the sulfonate S group in PSS, respectively.[47]

The energy separation between the S $2p_3/_2$ and S $2p_1/_2$ components was approximately 1.2 eV,[48] consistent with reported values for PEDOT:PSS. The Pt 4f spectrum (Figure 5F) exhibited doublet signals at 71.1/74.3 eV and 72.5/76.3 eV, assigned to metallic state Pt^0 and oxidized state Pt^{2+} species, respectively.[49] The coexistence of these mixed-valence Pt states, together with the PEDOT:PSS matrix, is indicative of the formation of a coating capable of efficient interfacial charge transport. After subsequent chitosan/GOx functionalization, increased O/C atomic ratio and pronounced enhancement of the N 1s signal (Figure S11) were observed, indicating the presence of the desired chitosan/GOx composite hydrogel on the SI-MNE surface.[50]

3.5. Electrochemical Performance for Glucose Detection

SI-MNE measures glucose using an enzyme-mediated electrochemical transduction mechanism (Figure 6A). A conformal multilayer architecture was constructed on the SI-MNE surface, comprising a GOx-embedded chitosan hydrogel as the enzymatic interface, a PEDOT:PSS/Pt composite as the catalytic layer, and an underlying carbon layer functioning as a continuous current collector. Glucose oxidation catalyzed by GOx proceeds through two redox steps. In the first step, d-glucose is oxidized to d-glucono-1,5-lactone, which is accompanied by reduction of the bound flavin adenine dinucleotide (FAD) prosthetic group within GOx to $FADH_2$, as described in eq 1:

$$\mathrm{D-glucose + GOx(FAD) \rightarrow d-glucono-1,5-lactone + GOx(FADH_2)} \quad (1)$$

subsequently, the reduced $FADH_2$ molecule reacts with dissolved O_2 present in phosphate-buffered saline (PBS),

https://doi.org/10.1021/acsami.6c10560
ACS Appl. Mater. Interfaces 2026, 18, 53922−53934

Downloaded from pubs.acs.org/aamick/article-pdf/18/39/53922/6861346l/am-2026-10560b.pdf by INHA UNIV user on 19 October 2026

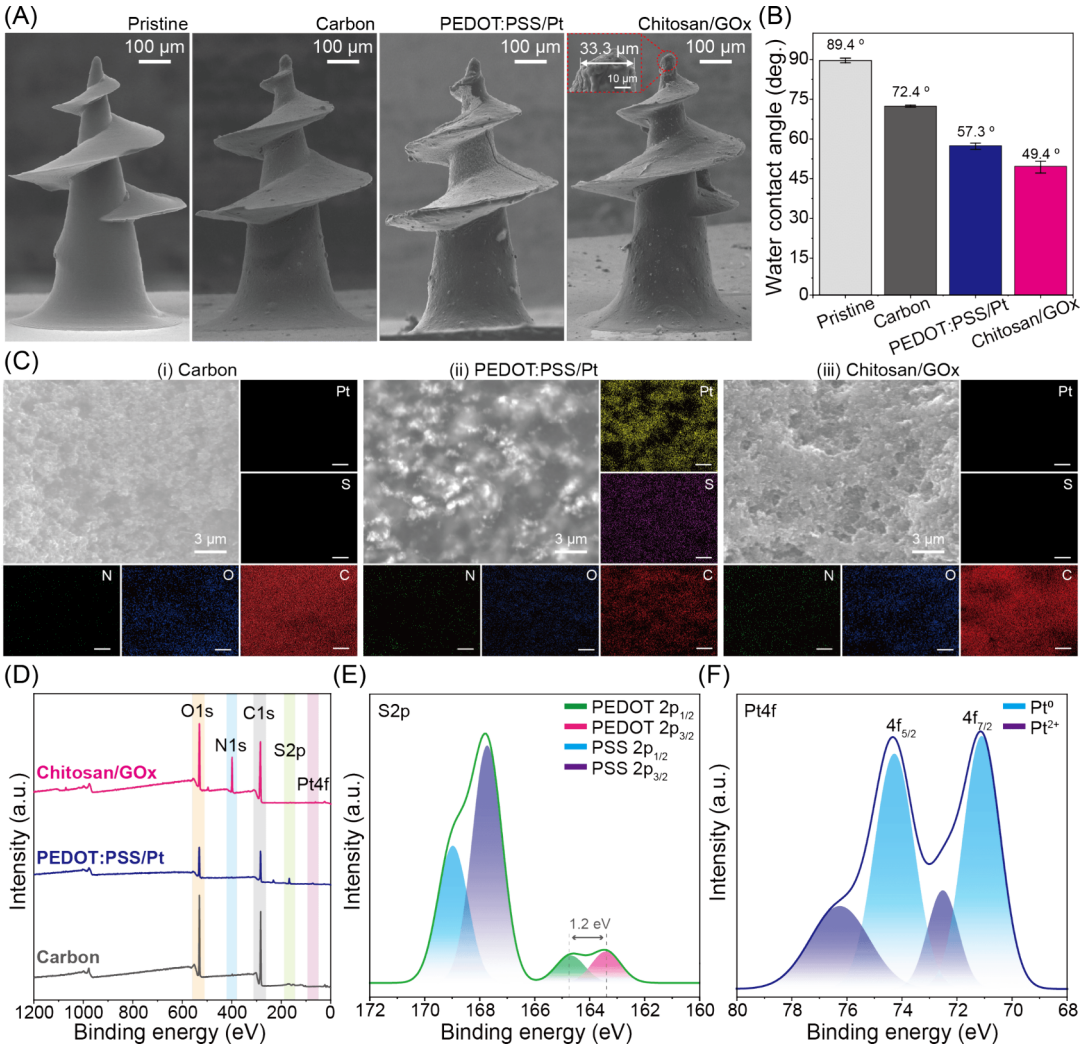


Figure 5. Sequential surface modification and physicochemical characterization of the SI-MNE. (A) Scanning electron microscopy (SEM) images and (B) WCA measurements at sequential surface-modification states: pristine, carbon-coated, PEDOT:PSS/Pt composite-coated, and chitosan/GOx-functionalized. The WCA measurements shown represent the mean of three independent samples ± the standard deviation. (C) SEM and corresponding EDS-based elemental surface mapping with: (i) carbon, (ii) PEDOT:PSS/Pt, and (iii) chitosan/GOx layers. Scale bars, 3 μm. (D) Wide-scan XPS spectra with peaks corresponding to C 1s, O 1s, N 1s, S 2p, and Pt 4f. (E) High-resolution S 2p spectrum showing doublet peaks at 163.4/164.7 eV and 167.7/169.0 eV, corresponding to the thiophene S in PEDOT and sulfonate S in PSS, respectively. (F) High-resolution Pt 4f spectrum exhibiting doublet signals at 71.1/74.3 eV and 72.5/76.3 eV, attributed to metallic Pt^0 and oxidized Pt^{2+} species, respectively.

producing H_2O_2, as described in eq 2:

$$GOx(FADH_2) + O_2 \rightarrow GOx(FAD) + H_2O_2 \quad (2)$$

the H_2O_2 produced during this process is then oxidized at the Pt nanoparticle catalytic sites distributed across the SI-MNE surface, as described in eq 3:

$$H_2O_2 \xrightarrow{Pt} 2H^+ + O_2 + 2e^- \quad (3)$$

the resulting electrons are transported through the carbon conductive layer, producing a glucose-dependent current that enables amperometric quantification of glucose concentrations.

Layer-specific responses were examined using relative current measurements performed after each step (Figure 6B). Stepwise additions of H_2O_2 and glucose were performed to independently assess catalytic and enzymatic activity. The carbon layer alone exhibited negligible current changes in response to both analytes, as expected. PEDOT:PSS/Pt layer deposition resulted in a measurable current upon H_2O_2 exposure, consistent with catalytic activity. Subsequent coating with GOx-embedded chitosan produced a pronounced glucose-induced current.

Building on the validated surface functionalization, we next measured electrochemical responses under stepwise glucose additions (Figure 6C and Figure S12). At a constant potential of 0.5 V, we measured stepwise increases in the drain current upon sequential addition of glucose over 1−100 mM. The current increased monotonically with glucose concentration. The corresponding calibration plot exhibited a linear relationship between response current and glucose concentration within the tested range, as described in eq 4:

$$y\,(\text{nA}) = 350.3\,[\text{glucose}]\,(\text{mM}) + 35.56 \text{ with } R^2 = 0.946 \quad (4)$$

https://doi.org/10.1021/acsami.6c10560
ACS Appl. Mater. Interfaces 2026, 18, 53922−53934

Downloaded from pubs.acs.org/aamick/article-pdf/18/39/53922/6861346l/am-2026-10560b.pdf by INHA UNIV user on 19 October 2026

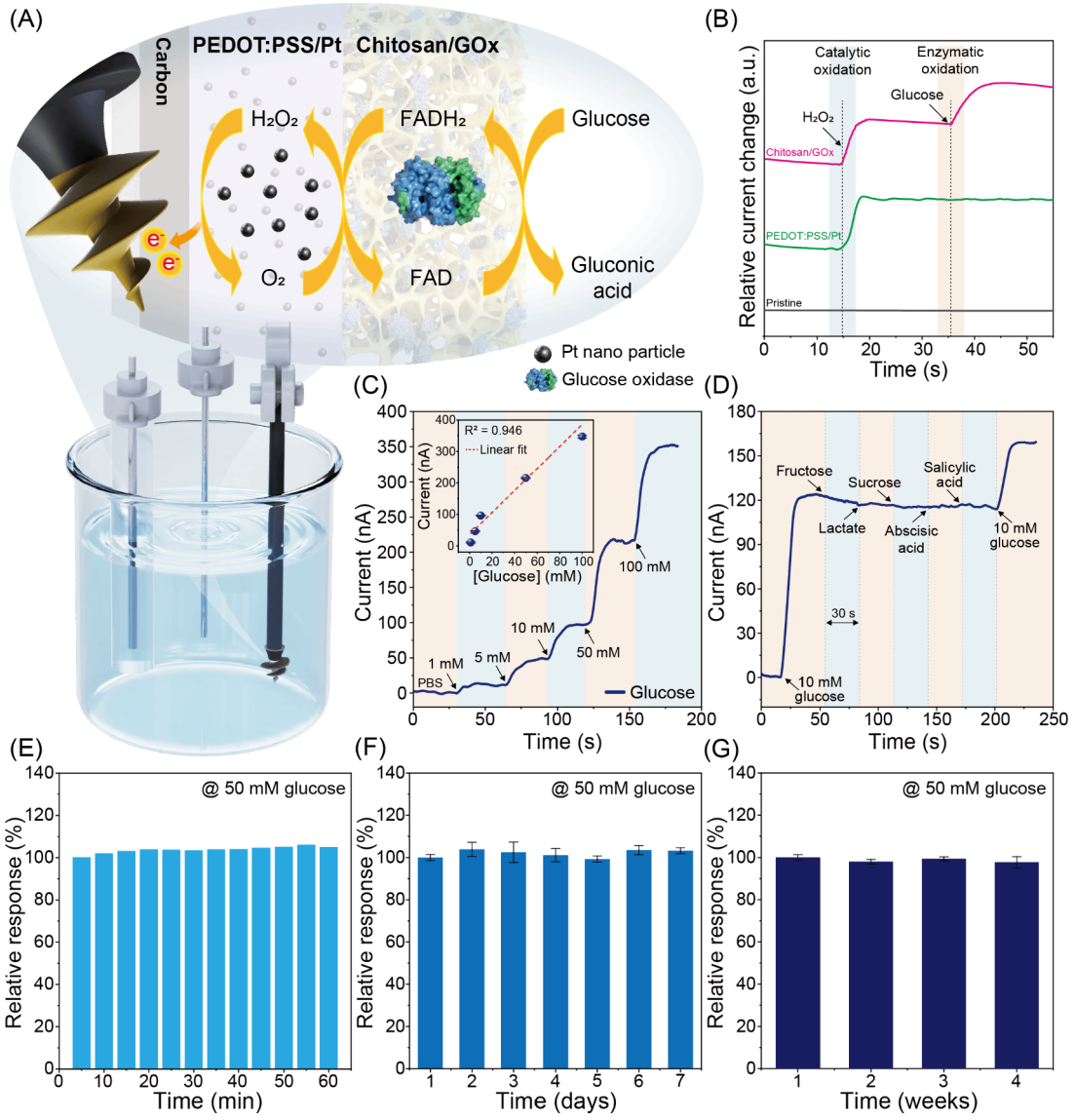


Figure 6. Electrochemical characteristics of the SI-MNE for glucose detection. (A) Schematic of the electrochemical interface: carbon base, PEDOT:PSS/Pt nanoparticle catalytic, and chitosan−GOx enzymatic layers. (B) Current responses illustrating the sequential emergence of catalytic and enzymatic oxidation upon layer-by-layer surface functionalization; a.u., arbitrary units. (C) Stepwise addition of glucose increases current. Inset: calibration plot showing correlation (linear $R^2 = 0.946$). (D) Selectivity measured by introducing 10 mM glucose, then known sap components applied at 5 mM, ending with an additional 1 mM glucose. (E, F) Relative currents measured (E) from 10 to 60 min at 5-min intervals and (F) at 24-h intervals over 7 d in PBS containing 50 mM glucose. (G) Relative currents measured in the presence of 50 mM glucose after 1−4 weeks of ambient storage. Error bars represent standard deviations.

When benchmarked against previously reported enzyme-based MNE glucose sensors, the SI-MNE had markedly higher sensitivity on a per-MNE basis while maintaining a broad range (Table S2). For application in plants, reliable glucose detection requires selectivity against coexisting saccharides and electroactive metabolites. To evaluate selectivity, representative sap-derived interferents (fructose, sucrose, lactate, abscisic acid, and salicylic acid) were each administered at 5 mM in 30 s intervals (Figure 6D); none produced a measurable current. These data demonstrate high selectivity in plant sap−relevant conditions. The SI-MNE response was also evaluated under different electrolyte ionic strengths (Figure S13). The relative response increased with increasing PBS concentration, accompanied by a decrease in the charge-transfer resistance.[51,52] In addition, the effects of pH and temperature on the sensor response were evaluated with 50 mM glucose (Figures S14 and S15). The sensor exhibited the highest response at pH 5 and a 40 °C, consistent with the reported pH- and temperature-dependent catalytic characteristics of GOx.[53−56]

To monitor glucose during prolonged operation, reproducibility was evaluated over time with repeated measurements with 50 mM glucose. We observed relative standard deviations (RSDs) of 1.49% over 60 min, 1.79% over a week, and 1.12% after 4 weeks of ambient storage (Figure 6E−G, respectively). Device-to-device reproducibility assessed after 4 weeks of ambient storage showed an RSD of 3.07% across five independently prepared SI-MNE (Figure S16). In addition to signa reproducibility, degradation was directly assessed

https://doi.org/10.1021/acsami.6c10560
ACS Appl. Mater. Interfaces 2026, 18, 53922−53934

Downloaded from pubs.acs.org/aamick/article-pdf/18/39/53922/6861346l/am-2026-10560b.pdf by INHA UNIV user on 19 October 2026

by comparing the responses of five independently prepared SI-MNEs before and after 7 days, which showed 99.6% signal retention (RSD 1.05%), confirming no meaningful performance loss (Figure S17). Collectively, these results demonstrate that SI-MNE is robust under extended operation and storage conditions.

3.6. Long-Term in Planta Glucose Monitoring with Minimal Tissue Disruption

Figure 7A and Figure S18 illustrate the experimental setup in naturally growing tomato plants maintained under ambient light−dark cycles. A conventional three-electrode configuration was implemented using SI-MNE as working, reference, and counter electrodes (Figure 7B); a cross-section of the petiole confirmed stable integration of the spiral-interlocking geometry within the tissue (Figure 7C). With this configuration, continuous amperometric measurements were conducted for 7 d (Figure 7D). Currents exhibited reproducible diurnal modulation; elevated during illuminated periods and reduced during darkness. These variations are consistent with both light-driven carbohydrate production during photosynthetically active phases and glucose consumption associated with respiratory metabolism in the dark. The persistence of this pattern over multiple cycles demonstrates that SI-MNE reliably tracks endogenous glucose dynamics in living plants over time. Because the prepared SI-MNE relies on a GOx-catalyzed enzymatic reaction, physiological variations in gaseous species should also be considered when interpreting the sensing results. In particular, dissolved O_2 serves as a co-substrate for enzymatic glucose oxidation and its local availability can vary during photosynthesis and respiration. Although such variations could influence enzyme kinetics, the physiological conditions used in this study were not expected to cause sufficient O_2 depletion to limit the enzymatic reaction. Carbon dioxide (CO_2), another key component associated with these physiological processes, may also influence the local physiological environment. Although the present study was conducted under ambient physiological conditions, an investigation of O_2 and CO_2 variations under controlled environmental conditions would elucidate their influence on long-term in planta glucose sensing. Beyond these physiological factors, SI-MNE was designed for continuous monitoring of relative glucose dynamics rather than absolute concentration determination. In the present study, the recorded signals were not independently cross-validated against an established analytical method; such destructive reference sampling, concomitant with the localized sensing volume of the sensor, is itself perturbative and technically challenging, precisely the limitation the SI-MNE is intended to overcome. Independent, quantitative validation of absolute tissue glucose levels therefore remains an important subject for future work.

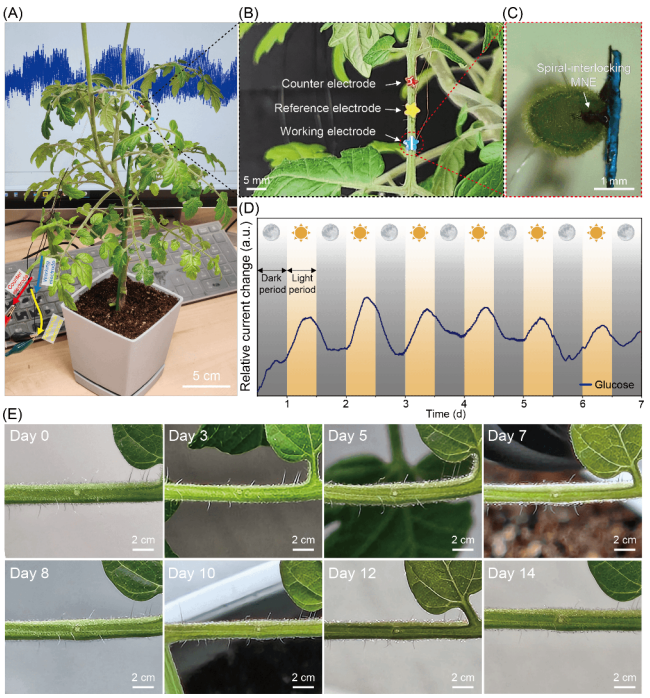


Figure 7. In situ plant glucose monitoring using the SI-MNE. (A) Experimental setup for continuous glucose monitoring in a living tomato plant. (B) Three-electrode configuration positioned on the tomato stem (working, reference, and counter electrodes). (C) Cross-sectional view of the insertion site, confirming stable penetration of the SI-MNE within the tissue. (D) 7 days glucose monitoring trace using amperometric measurements, showing cyclic fluctuations synchronized with day−night transitions. (E) Optical images of the insertion site over 14 days, indicating minimal tissue damage and gradual recovery.

Finally, we evaluated MNE-induced wound recovery in tomato petioles (Figure 7E). Following removal of the SI-MNE, microporous features were observed at the petiole surface at the insertion site. Over 14 d, these insertion-induced openings progressively decreased in size, accompanied by restored petiole surface continuity, without observable evidence of tissue necrosis or structural degradation. In addition, during this interval both the treated petioles and adjacent leaves exhibited normal growth without visible morphological abnormalities. Such favorable characteristics can be attributed to the MNE configuration, which confines tissue penetration to a limited region to minimize damage. Collectively, these observations indicate effective wound closure following microneedle removal and support the minimally invasive nature of the SI-MNE for prolonged use in plant tissue.

4. CONCLUSIONS

In this study, a SI-MNE glucose sensor with a mechanically engineered spiral-interlocking geometry was developed for long-term, continuous glucose monitoring in plants. To validate the mechanical functionality of the designed geometry, its insertion behavior was evaluated by cyclic voltammetry through changes in interfacial capacitance, whereas pull-out resistance was quantified via mechanical testing, revealing approximately 10-fold higher resistance than found with conventional designs. In parallel, OCT was employed to directly visualize SI-MN insertion within plant tissues. Formation of the multilayer SI-MNE interface was confirmed via surface analysis, establishing a chemical basis for concentration-dependent amperometric glucose detection over a broad dynamic range up to 100 mM, with a sensitivity of 350.3 nA/mM. In addition, shelf-life stability was assessed during ambient storage for 4 weeks, whereby five independently prepared SI-MNE exhibited a relative standard deviation of 3.07%. Building upon these electrochemical characterizations, continuous in planta measurements in living tomato plants demonstrated stable glucose monitoring over 7 consecutive days under light−dark cycles. Collectively, the SI-MNE approach enables mechanically robust and

Downloaded from pubs.acs.org/aamick/article-pdf/18/39/53922/6861346l/am-2026-10560b.pdf by INHA UNIV user on 19 October 2026

https://doi.org/10.1021/acsami.6c10560
ACS Appl. Mater. Interfaces 2026, 18, 53922−53934

electrochemically reliable continuous in situ monitoring of glucose dynamics in living plants.

■ ASSOCIATED CONTENT

Data Availability Statement

This study did not generate/analyze any datasets/code and did not generate new unique reagents. Further information and requests for resources and reagents should be directed to Dae Yu Kim (dyukim@inha.ac.kr).

Supporting Information

The Supporting Information is available free of charge at https://pubs.acs.org/doi/10.1021/acsami.6c10560.

Geometric dimensions of the SI-MN; cyclic voltammetry curves at cumulative rotation angles during rotational insertion; conceptual modeling of light penetration for the SI-MNE−inserted petiole; OCT volumetric and *xy*-plane images of the SI-MNE−inserted petiole; axial compression setup for mechanical stability evaluation; comparison of pull-out force between conical and SI-MN; structural integrity of the SI-MN after different removal conditions; high-resolution C1s XPS spectra of the carbon-, PEDOT:PSS/Pt-, and chitosan/GOx-modified surfaces; XPS survey spectra after sequential surface coating; amperometric responses to stepwise glucose additions; effect of PBS concentration on electrochemical performance; relative amperometric response as a function of pH; relative amperometric response as a function of temperature; relative responses of five SI-MN after four weeks; relative responses of five independently prepared SI-MNE measured before and after 7 days; schematic of the three-electrode connections for the in planta test; optical images of the PDMS negative mold and PDMS MN; schematic of the custom-built OCT system; water contact angle measurement with surface modification; and comparison of the performance parameters of enzyme-based glucose sensors using MNs (DOCX)

Dynamic pull-out process of the SI-MNE under a 20 g load (MP4)

■ AUTHOR INFORMATION

Corresponding Author

Dae Yu Kim – *Department of Electrical and Computer Engineering, Inha University, Incheon 22212, Republic of Korea; Center for Sensor Systems, Inha University, Incheon 22212, Republic of Korea; Inha Research Institute for Aerospace Medicine, Inha University, Incheon 22212, Republic of Korea;* orcid.org/0000-0003-4200-5670; Email: dyukim@inha.ac.kr

Authors

Chuljin Hwang – *Department of Electrical and Computer Engineering, Inha University, Incheon 22212, Republic of Korea;* orcid.org/0000-0001-5646-2077

Ju Hyeon Kim – *Department of Mechanical Engineering, Inha University, Incheon 22212, Republic of Korea*

Hang Chan Jo – *Department of Electrical and Computer Engineering, Inha University, Incheon 22212, Republic of Korea*

Complete contact information is available at: https://pubs.acs.org/doi/10.1021/acsami.6c10560

Author Contributions

#C.H. and J.K. contributed equally to this work. C. Hwang and J.H. Kim designed the experiments. C. Hwang, J.H. Kim, and H.C. Jo performed the experiments and collated the data. C. Hwang, J.H. Kim, and H.C. Jo analyzed the data. C. Hwang wrote the original draft. D.Y. Kim conducted project administration and reviewed the manuscript.

Notes

The authors declare no competing financial interest.

■ ACKNOWLEDGMENTS

This study was supported by grants from the National Research Foundation of Korea (NRF) (RS-2018-NR031065, RS-2024-00460600, and RS-2025-00559359). This research was supported by Korea Institute for Advancement of Technology (KIAT) grant funded by the Korea Government (MOTIE) (RS-2022-KI002581, HRD Program for Industrial Innovation).

■ REFERENCES

(1) Bodirsky, B. L.; Beier, F.; Humpenöder, F.; Leip, D.; Crawford, M. S.; Chen, D. M.-C.; von Jeetze, P.; Springmann, M.; Soergel, B.; Nicholls, Z.; Strefler, J.; Lewis, J.; Heinke, J.; Müller, C.; Karstens, K.; Weindl, I.; Stevanović, M.; Rein, P.; Sauer, P.; Mishra, A.; Bacca, E. J. M.; Köberle, A. C.; Wang, X.; Singh, V.; Hunecke, C.; Collignon, Q.; Schreinemachers, P.; Dietz, S.; Kanbur, R.; Dietrich, J. P.; Lotze-Campen, H.; Popp, A. A Food System Transformation Pathway Reconciles 1.5 °C Global Warming with Improved Health, Environment and Social Inclusion. *Nat. Food* **2025**, *6* (12), 1133−1152.

(2) Schmidhuber, J.; Tubiello, F. N. Global Food Security under Climate Change. *Proc. Natl. Acad. Sci.* **2007**, *104* (50), 19703−19708.

(3) Islam, S. Agriculture, Food Security, and Sustainability: A Review. *Explor. Foods Foodomics* **2025**, *3*, No. 101082.

(4) Rizzo, D. M.; Lichtveld, M.; Mazet, J. A. K.; Togami, E.; Miller, S. A. Plant Health and Its Effects on Food Safety and Security in a One Health Framework: Four Case Studies. *One Health Outlook* **2021**, *3*, 6.

(5) Food and Agriculture Organization. *International Year of Plant Health 2020 | FAO | Food and Agriculture Organization of the United Nations*, https://www.fao.org/plant-health-2020/home/en/ (accessed 2025-12-24).

(6) Ray, D. K.; Mueller, N. D.; West, P. C.; Foley, J. A. Yield Trends Are Insufficient to Double Global Crop Production by 2050. *PLoS ONE* **2013**, *8* (6), No. e66428.

(7) van Dijk, M.; Morley, T.; Rau, M. L.; Saghai, Y. A Meta-Analysis of Projected Global Food Demand and Population at Risk of Hunger for the Period 2010−2050. *Nat. Food* **2021**, *2* (7), 494−501.

(8) Razzaq, A.; Sadia, B.; Raza, A.; Khalid Hameed, M.; Saleem, F. Metabolomics: A Way Forward for Crop Improvement. *Metabolites* **2019**, *9* (12), No. 303.

(9) Manickam, S.; Rajagopalan, V. R.; Kambale, R.; Rajasekaran, R.; Kanagarajan, S.; Muthurajan, R. Plant Metabolomics: Current Initiatives and Future Prospects. *Curr. Issues Mol. Biol.* **2023**, *45* (11), 8894−8906.

(10) Rogers, J. K.; Church, G. M. Genetically Encoded Sensors Enable Real-Time Observation of Metabolite Production. *Proc. Natl. Acad. Sci.* **2016**, *113* (9), 2388−2393.

(11) Wagner, S.; Meyer, A. J. Illuminating Plant Metabolism with Genetically Encoded Biosensors. *J. Plant Physiol.* **2025**, *311*, No. 154498.

Downloaded from pubs.acs.org/aamick/article-pdf/18/39/53922/6861346l/am-2026-10560b.pdf by INHA UNIV user on 19 October 2026

(12) Kuila, T.; Bose, S.; Khanra, P.; Mishra, A. K.; Kim, N. H.; Lee, J. H. Recent Advances in Graphene-Based Biosensors. *Biosens. Bioelectron.* **2011**, *26* (12), 4637−4648.
(13) Penhaul Smith, J. K.; Hughes, A. D.; McEvoy, L.; Thornton, B.; Day, J. G. The Carbon Partitioning of Glucose and DIC in Mixotrophic, Heterotrophic and Photoautotrophic Cultures of Tetraselmis Suecica. *Biotechnol. Lett.* **2021**, *43* (3), 729−743.
(14) Zhang, S.; Sun, J.; Feng, D.; Sun, H.; Cui, J.; Zeng, X.; Wu, Y.; Luan, G.; Lu, X. Unlocking the Potentials of Cyanobacterial Photosynthesis for Directly Converting Carbon Dioxide into Glucose. *Nat. Commun.* **2023**, *14* (1), 3425.
(15) Siddiqui, H.; Sami, F.; Hayat, S. Glucose: Sweet or Bitter Effects in Plants-a Review on Current and Future Perspective. *Carbohydr. Res.* **2020**, *487*, No. 107884.
(16) Vaulont, S.; Vasseur-Cognet, M.; Kahn, A. Glucose Regulation of Gene Transcription. *J. Biol. Chem.* **2000**, *275* (41), 31555−31558.
(17) Yamada, K.; Mine, A. Sugar Coordinates Plant Defense Signaling. *Sci. Adv.* **2024**, *10* (4), No. eadk4131.
(18) Sami, F.; Siddiqui, H.; Hayat, S. Interaction of Glucose and Phytohormone Signaling in Plants. *Plant Physiol. Biochem.* **2019**, *135*, 119−126.
(19) Kushwah, S.; Jones, A. M.; Laxmi, A. Cytokinin Interplay with Ethylene, Auxin, and Glucose Signaling Controls Arabidopsis Seedling Root Directional Growth1[W][OA]. *Plant Physiol.* **2011**, *156* (4), 1851−1866.
(20) Mishra, B. S.; Singh, M.; Aggrawal, P.; Laxmi, A. Glucose and Auxin Signaling Interaction in Controlling Arabidopsis Thaliana Seedlings Root Growth and Development. *PloS ONE* **2009**, *4* (2), No. e4502.
(21) Kushwah, S.; Laxmi, A. The Interaction between Glucose and Cytokinin Signal Transduction Pathway in Arabidopsis Thaliana. *Plant Cell Environ.* **2014**, *37* (1), 235−253.
(22) Du, F. Epigenetic Reprogramming by Glucose-TOR Signaling Controls Plant Development. *Mol. Plant* **2022**, *15* (11), 1651−1652.
(23) Janse van Rensburg, H. C.; Van den Ende, W. UDP-Glucose: A Potential Signaling Molecule in Plants? *Front. Plant Sci.* **2018**, *8*, 1.
(24) Wingler, A.; Henriques, R. Sugars and the Speed of Life—Metabolic Signals That Determine Plant Growth, Development and Death. *Physiol. Plant.* **2022**, *174* (2), No. e13656.
(25) Lastdrager, J.; Hanson, J.; Smeekens, S. Sugar Signals and the Control of Plant Growth and Development. *J. Exp. Bot.* **2014**, *65* (3), 799−807.
(26) Sun, X. Glucose Detection through Surface-Enhanced Raman Spectroscopy: A Review. *Anal. Chim. Acta* **2022**, *1206*, No. 339226.
(27) Luo, F.; Lin, Y.; Zheng, L.; Lin, X.; Chi, Y. Encapsulation of Hemin in Metal−Organic Frameworks for Catalyzing the Chemiluminescence Reaction of the H_2O_2−Luminol System and Detecting Glucose in the Neutral Condition. *ACS Appl. Mater. Interfaces* **2015**, *7* (21), 11322−11329.
(28) Chen, S.; Zheng, H.; Wang, J.; Hou, J.; He, Q.; Liu, H.; Xiong, C.; Kong, X.; Nie, Z. Carbon Nanodots As a Matrix for the Analysis of Low-Molecular-Weight Molecules in Both Positive- and Negative-Ion Matrix-Assisted Laser Desorption/Ionization Time-of-Flight Mass Spectrometry and Quantification of Glucose and Uric Acid in Real Samples. *Anal. Chem.* **2013**, *85* (14), 6646−6652.
(29) Czarnik, A. W.; James, T. D. Fluorescent Chemosensors in the Creation of a Commercially Available Continuous Glucose Monitor. *ACS Sens.* **2024**, *9* (12), 6320−6326.
(30) Lyu, S.; Dong, Z.; Xu, X.; Bei, H.-P.; Yuen, H.-Y.; James Cheung, C.-W.; Wong, M.-S.; He, Y.; Zhao, X. Going below and beyond the Surface: Microneedle Structure, Materials, Drugs, Fabrication, and Applications for Wound Healing and Tissue Regeneration. *Bioact. Mater.* **2023**, *27*, 303−326.
(31) Kim, H. Y.; Kim, H. B.; Park, J.-H.; Kim, M. J.; Byun, J.-H.; Oh, S. H. Simultaneous Regeneration of Epithelial and Bone Tissue Using a Multifunctional Film with Leaf-Stacked Structures and Growth Factors. *Biomater. Sci.* **2025**, *14* (3), 894−906.
(32) Wang, Y.; Wu, Y.; Lei, Y. Microneedle-Based Glucose Monitoring: A Review from Sampling Methods to Wearable Biosensors. *Biomater. Sci.* **2023**, *11* (17), 5727−5757.
(33) Hu, Y.; Chatzilakou, E.; Pan, Z.; Traverso, G.; Yetisen, A. K. Microneedle Sensors for Point-of-Care Diagnostics. *Adv. Sci.* **2024**, *11* (12), No. 2306560.
(34) Jones, W. P.; Kinghorn, A. D.Extraction of Plant Secondary Metabolites. In *Natural Products Isolation*; Sarker, S. D., Latif, Z., Gray, A. I., Eds.; Humana Press: Totowa, NJ, **2005**; pp 323−351.
(35) Pontius, K.; Semenova, D.; Silina, Y. E.; Gernaey, K. V.; Junicke, H. Automated Electrochemical Glucose Biosensor Platform as an Efficient Tool Toward On-Line Fermentation Monitoring: Novel Application Approaches and Insights. *Front. Bioeng. Biotechnol.* **2020**, *8*, No. 436.
(36) Fan, C.-X.; Wang, Z.; Wang, Z.-H.; Wang, A.-W.; Wang, Z.-Y.; Huang, L. A Microneedle Sensor for *in-Vivo* Sodium Ion Detection in Plants. *Anal. Chim. Acta* **2025**, *1352*, No. 343892.
(37) Bukhamsin, A.; Moussi, K.; Tao, R.; Lubineau, G.; Blilou, I.; Salama, K. N.; Kosel, J. Robust, Long-Term, and Exceptionally Sensitive Microneedle-Based Bioimpedance Sensor for Precision Farming. *Adv. Sci.* **2021**, *8* (16), No. 2101261.
(38) Fiorello, I.; Meder, F.; Mondini, A.; Sinibaldi, E.; Filippeschi, C.; Tricinci, O.; Mazzolai, B. Plant-like Hooked Miniature Machines for on-Leaf Sensing and Delivery. *Commun. Mater.* **2021**, *2* (1), 103.
(39) Wu, S.; Li, Y.; Wang, Q.; Cai, Y.; Teng, P.; Li, W.; Zhang, F.; Xu, L.-P.; Wang, S. Wearable Plant Sensing Devices for Health Monitoring. *Wearable Electron.* **2025**, *2*, 100−115.
(40) Chen, H.; Zhou, S.; Chen, J.; Zhou, J.; Fan, K.; Pan, Y.; Ping, J. An Integrated Plant Glucose Monitoring System Based on Microneedle-Enabled Electrochemical Sensor. *Biosens. Bioelectron.* **2024**, *248*, No. 115964.
(41) Yun, J.; Park, S.; Kim, N. W.; Kang, J.; Kim, S.; Hur, S.; Ryu, W. K-Doped Co3O4-Decorated Microneedle Clip for Non-Enzymatic Glucose Detection in Plant Health Monitoring. *Sens. Actuators B* **2025**, *435*, No. 137600.
(42) Banan, A. R. Solvent Free UV Curable Waterborne Polyurethane Acrylate Coatings with Enhanced Hydrophobicity Induced by a Semi Interpenetrating Polymer Network. *Sci. Rep.* **2025**, *15* (1), 21844.
(43) Ji, J.; Xiao, J.; Zhang, F.; Wang, Z.; Zhou, T.; Niu, X.; Zhang, W.; Sang, S.; Chai, X.; Yan, S. A Wearable Enzyme Sensor Enabled by the Floating-Gate OECT with Poly(Benzimidazobenzophenanthroline) as the Catalytic Layer. *J. Nanobiotechnology* **2025**, *23* (1), 120.
(44) Gebremichael, Z. T.; Ugokwe, C.; Alam, S.; Stumpf, S.; Diegel, M.; Schubert, U. S.; Hoppe, H. How Varying Surface Wettability of Different PEDOT:PSS Formulations and Their Mixtures Affects Perovskite Crystallization and the Efficiency of Inverted Perovskite Solar Cells. *RSC Adv.* **2022**, *12* (39), 25593−25604.
(45) Dhekra, A.; Khaled, H.; Mina, S.; Mustapha, M.; Ali, O. Immobilization of Glucose Oxidase in Anthracene-Based Semi-Conducting Polymer: Application on Glucose Biosensing. *J. Bioeng. Biomed. Sci.* **2017**, *07* (05).
(46) Hu, L.; Li, M.; Yang, K.; Xiong, Z.; Yang, B.; Wang, M.; Tang, X.; Zang, Z.; Liu, X.; Li, B.; Xiao, Z.; Lu, S.; Gong, H.; Ouyang, J.; Sun, K. PEDOT:PSS Monolayers to Enhance the Hole Extraction and Stability of Perovskite Solar Cells. *J. Mater. Chem. A* **2018**, *6* (34), 16583−16589.
(47) Kim, G.-H.; Shao, L.; Zhang, K.; Pipe, K. P. Engineered Doping of Organic Semiconductors for Enhanced Thermoelectric Efficiency. *Nat. Mater.* **2013**, *12* (8), 719−723.
(48) Mahato, S. Composition Analysis of Two Different PEDOT:PSS Commercial Products Used as an Interface Layer in Au/n-Si Schottky Diode. *RSC Adv* **2017**, *7* (74), 47125−47131.
(49) Artigues, M.; Gilabert-Porres, J.; Texidó, R.; Borrós, S.; Abellà, J.; Colominas, S.; Artigues, M.; Gilabert-Porres, J.; Texidó, R.; Borrós, S.; Abellà, J.; Colominas, S. Analytical Parameters of a Novel Glucose Biosensor Based on Grafted PFM as a Covalent Immobilization Technique. *Sensors* **2021**, *21* (12).

Downloaded from pubs.acs.org/aamick/article-pdf/18/39/53922/6861346l/am-2026-10560b.pdf by INHA UNIV user on 19 October 2026

https://doi.org/10.1021/acsami.6c10560
ACS Appl. Mater. Interfaces 2026, 18, 53922−53934

(50) Yang, L.; Hu, L.; Zhao, S.; Zhao, R.; Gu, W.; Jin, T. Immobilization of Glucose Oxidase Based on the Sodium Alginate-Modified Products of a Functionalized Metal Organic Framework and the Application for One-Pot Analysis of Glucose. *J. Coord. Chem.* **2019**, *72* (3), 428−437.
(51) Fontananova, E.; Zhang, W.; Nicotera, I.; Simari, C.; van Baak, W.; Di Profio, G.; Curcio, E.; Drioli, E. Probing Membrane and Interface Properties in Concentrated Electrolyte Solutions. *J. Membr. Sci.* **2014**, *459*, 177−189.
(52) Bohinc, K.; Kralj-Iglič, V.; Iglič, A. Thickness of Electrical Double Layer. Effect of Ion Size. *Electrochimica Acta* **2001**, *46* (19), 3033−3040.
(53) Bhatti, H. N.; Madeeha, M.; Asgher, M.; Batool, N. Purification and Thermodynamic Characterization of Glucose Oxidase from a Newly Isolated Strain of Aspergillus Niger. *Can. J. Microbiol.* **2006**, *52* (6), 519−524.
(54) Kim, D.-M.; Cho, S. J.; Cho, C.-H.; Kim, K. B.; Kim, M.-Y.; Shim, Y.-B. Disposable All-Solid-State pH and Glucose Sensors Based on Conductive Polymer Covered Hierarchical AuZn Oxide. *Biosens. Bioelectron.* **2016**, *79*, 165−172.
(55) Adib, M. R.; Barrett, C.; O'Sullivan, S.; Flynn, A.; McFadden, M.; Kennedy, E.; O'Riordan, A. In Situ pH-Controlled Electrochemical Sensors for Glucose and pH Detection in Calf Saliva. *Biosens. Bioelectron.* **2025**, *275*, No. 117234.
(56) Zare, H.; Najafpour, G.; Jahanshahi, M.; Rahimnejad, M.; Rezvani, M. *Highly Stable Biosensor Based on Glucose Oxidase Immobilized in Chitosan Film for Diagnosis of Diabetes*, **2017**.

Downloaded from pubs.acs.org/aamick/article-pdf/18/39/53922/6861346l/am-2026-10560b.pdf by INHA UNIV user on 19 October 2026

https://doi.org/10.1021/acsami.6c10560
ACS Appl. Mater. Interfaces 2026, 18, 53922−53934